

Electronic supplementary materials

For <https://doi.org/10.1631/jzus.A2200238>

Numerical investigations of the failure mechanism evolution of rock-like disc specimens containing unfilled or filled flaws

Tian WANG¹, Jian WANG¹, Sheng JIANG^{1,2}, Jiahe ZHANG¹

¹College of Water Conservancy and Hydropower Engineering, Hohai University, Nanjing 210098, China

²School of Civil Engineering, The University of Sydney, Sydney, NSW 2006, Australia

S1 Governing equations

The governing equations, the continuity equation and the momentum equation, are the behavioral criteria that the object must obey in every step of the calculation iteration, which guarantee the conservations of mass and momentum. They are expressed as:

$$\frac{d\rho}{dt} = -\rho \nabla \cdot \mathbf{v}, \quad (\text{S1})$$

$$\frac{d\mathbf{v}}{dt} = \frac{1}{\rho} \nabla \cdot \boldsymbol{\sigma} + \mathbf{b}, \quad (\text{S2})$$

where ρ , \mathbf{v} , $\boldsymbol{\sigma}$, and \mathbf{b} denote respectively the density, the velocity vector, the stress vector and the corresponding acceleration vector due to external forces for the solid.

S2 SPH approximation

In the SPH modeling, the problem geometry is discretized into a finite number of particles, in which each particle carries its own field variables, such as velocity, density and stress, etc. Particles interact with their neighboring particles via the smoothing kernel. Each particle has a support domain Ω , specified by the radius of the smoothing kernel h . h is also denoted as a smoothing length.

Based on the integral interpolation, the properties of a particle can be approximately expressed by summarizing the properties of its surrounding particles within the smoothing range (Monaghan, 2005), as follows:

$$\langle f(\mathbf{x}_i) \rangle = \sum_{j=1}^N \frac{m_j}{\rho_j} f(\mathbf{x}_j) W(\mathbf{x}_i - \mathbf{x}_j, h), \quad (\text{S3})$$

where $f(\mathbf{x}_i)$ is the field variable of particle i at position \mathbf{x}_i , N is the total number of neighboring particles of particle i within the supporting domain Ω , W is the smoothing kernel function, h is the smoothing length, m_j and ρ_j are the mass and density values of particle j in the support domain Ω , respectively and the angle bracket $\langle \rangle$ represents the kernel approximation operator.

The partial derivative form of the field variable $f(\mathbf{x}_i)$ is expressed by the method of summation as follows:

$$\langle \nabla \cdot f(\mathbf{x}_i) \rangle = \sum_{j=1}^N m_j \frac{f(\mathbf{x}_j)}{\rho_j} \cdot \nabla W(\mathbf{x}_i - \mathbf{x}_j, h), \quad (\text{S4})$$

in which $\nabla W(\mathbf{x}_i - \mathbf{x}_j, h)$ is the gradient of the kernel function $W(\mathbf{x}_i - \mathbf{x}_j, h)$, evaluated at the location of \mathbf{x}_i .

The symmetric form of the kernel function proposed by Libersky et al. (1993) to generate a more accurate partial derivative form of the field variable $f(\mathbf{x}_i)$ is:

$$\langle \nabla \cdot f(\mathbf{x}_i) \rangle = \sum_{j=1}^N \frac{m_j}{\rho_j} (f(\mathbf{x}_j) - f(\mathbf{x}_i)) \cdot \nabla W(\mathbf{x}_i - \mathbf{x}_j, h). \quad (\text{S5})$$

S3 Tensile instability

In this paper, many techniques, such as artificial stress and the stress point method, are adopted to avoid tensile instability in the simulation. When SPH is applied to solid mechanics, a repulsive force is introduced when the particles come close to each other so as to simulate the interaction of atoms. When the particle is under tension, there will be attractions between particles which tend to result in clumps of particles. There are a variety of solutions for tensile instability: the stress point method, Lagrangian kernels (Rabczuk et al., 2004), CSPM mentioned in Section 2.1, the artificial stress method and the conservative smoothing approach.

The problem of the zero-energy mode is encountered when using SPH to calculate derivatives. To solve the problem of zero-energy mode, Dyka et al. (1997) used the stress point method to test its efficiency in solving the tension instability problem of SPH. The method uses two types of particles to solve the problem: stress points to calculate the stress and velocity particles to calculate momentum. These particles exchange constant variables in the calculation. Tensile instability can be avoided with stress points and Lagrangian kernels, while Eulerian kernels distort the domain of material instability (Belytschko et al., 2000; Belytschko and Xiao, 2002). Note that in SPH, the zero-energy mode occurs only in very special variable distribution fields. In the case of irregular particle distribution, the zero-energy mode does not generally occur. For the sake of simplification, the details of stress point and artificial stress implementation can be found in Vignjevic et al. (2000) and Monaghan (2000), respectively.

S4 The elastoplastic constitutive model for rock-like materials

The ideal elastoplastic constitutive model, assumes that the total strain and its increment can be divided into elastic deformation and plastic deformation:

$$\boldsymbol{\varepsilon}^{\alpha\beta} = \boldsymbol{\varepsilon}_e^{\alpha\beta} + \boldsymbol{\varepsilon}_p^{\alpha\beta}, \quad (\text{S6})$$

where α and β denote the Cartesian components with the Einstein convention applied to repeated indices; $\varepsilon_e^{\alpha\beta}$ determined by elastic theory stands for the elastic strain tensor and $\varepsilon_p^{\alpha\beta}$ stands for the plastic strain tensor, which needs to be deduced by plastic strain increment theory.

The elastic strain rate tensor $\dot{\varepsilon}_e^{\alpha\beta}$ is derived by Hooke's law:

$$\dot{\varepsilon}_e^{\alpha\beta} = \frac{\dot{s}^{\alpha\beta}}{2G} + \frac{1-2\nu}{3E} \dot{\sigma}^{\gamma\gamma} \delta^{\alpha\beta}, \quad (\text{S7})$$

in which $\dot{s}^{\alpha\beta}$ is the deviatoric stress rate tensor, $\dot{\sigma}^{\gamma\gamma}$ is the sum of the three normal stress rate components, i.e. $\dot{\sigma}^{\gamma\gamma} = \dot{\sigma}^{xx} + \dot{\sigma}^{yy} + \dot{\sigma}^{zz}$, G is the shear modulus, ν is the Poisson's ratio, E is the Young's modulus, and $\delta^{\alpha\beta}$ is the Kronecker's delta.

The plastic strain rate tensor $\dot{\varepsilon}_p^{\alpha\beta}$ is expressed by the gradient of the plastic potential function with respect to stress:

$$\dot{\varepsilon}_p^{\alpha\beta} = \dot{\lambda} \frac{\partial g}{\partial \sigma^{\alpha\beta}}, \quad (\text{S8})$$

with $\dot{\lambda}$ and g denoting the change rate of the plastic multiplier λ and the plastic potential function, respectively.

S5 Drucker-Prager model

The plastic potential function g specifies the stress-strain relationship. There are generally two kinds of plastic flow rules, namely, the associated flow rule and the non-associated flow rule. The non-associated flow rule is that the plastic potential function is not equal to the yield function:

$$g = \sqrt{J_2} + \bar{\eta} p(\sigma), \quad (\text{S9})$$

where $\bar{\eta} = \frac{6 \sin \psi}{\sqrt{3}(3 - \sin \psi)}$ is the coefficient related to the dilatancy angle ψ , and $p(\sigma)$ is the hydrostatic pressure.

A D-P model can be used to determine the residual stress state of particles after shear failure. Considering the problem of large deformation, the strain rate of the elastic-plastic model should adopt the Jaumann stress rate in the calculation. The stress-strain expression of the D-P model for non-associated flow rule is:

$$\dot{\sigma}^{\alpha\beta} = \sigma^{\alpha\gamma} \dot{\omega}^{\beta\gamma} + \sigma^{\gamma\beta} \dot{\omega}^{\alpha\gamma} + 2G\dot{\varepsilon}_e^{\alpha\beta} + K\dot{\varepsilon}^{\gamma\gamma} \delta^{\alpha\beta} - \dot{\lambda} \left[9K \sin \psi \delta^{\alpha\beta} + \frac{G}{\sqrt{J_2}} s^{\alpha\beta} \right], \quad (\text{S10})$$

where $\dot{\sigma}^{\alpha\beta}$ and $s^{\alpha\beta}$ are the stress rate tensor and the deviator stress tensor, $\dot{\varepsilon}^{\alpha\beta}$ and $e^{\alpha\beta}$ are the strain rate tensor and the deviator strain rate tensor, $\dot{\omega}^{\alpha\beta}$ is the rotation rate tensor, K is the elastic bulk modulus and $\dot{\lambda}$ is the rate of change of the plastic multiplier. When $\dot{\lambda} = 0$, Eq. (S10) is a linear elastic constitutive model.

S6 Validation of the SPH method accuracy

In this paper, the accuracy of SPH method is verified by simulation of the Brazilian disc model and the penny-shaped crack model.

S6.1 Brazilian disc

For an elastic homogeneous disc balanced by a uniformly distributed vertically radial load P , Hondros (1959) offers the analytical solution of the distribution of horizontal stress σ_{xx} and vertical stress σ_{yy} on the y axis in the disc:

$$\sigma_{xx}(0, y) = \frac{2P}{\pi} \left[\frac{\left(1 - \frac{y^2}{R^2}\right) \sin 2\phi}{1 - \frac{y^2}{R^2 \cos 2\phi} + \frac{y^4}{R^4}} - \tan^{-1} \left(\frac{1 + \frac{y^2}{R^2}}{1 - \frac{y^2}{R^2}} \right) \tan \phi \right], \quad (\text{S11})$$

$$\sigma_{yy}(0, y) = \frac{2P}{\pi} \left[\frac{\left(1 - \frac{y^2}{R^2}\right) \sin 2\phi}{1 - \frac{y^2}{R^2 \cos 2\phi} + \frac{y^4}{R^4}} + \tan^{-1} \left(\frac{1 + \frac{y^2}{R^2}}{1 - \frac{y^2}{R^2}} \right) \tan \phi \right], \quad (\text{S12})$$

in which the loading angle 2ϕ should not exceed 20° , R is the disc radius.

The schematic of the SPH model is given in Fig. S1. The disc radius is 20 mm. The disc is subjected to a uniform stress load of 20 MPa from an upper panel at a loading angle of 13.8° . The initial particle distance is set as 0.6 mm with a time step of 1.228×10^{-7} s. Consequently, the total numbers of velocity particles and stress particles are 3505 and 3480, respectively. Fig. S2 is the arrangement of velocity particles and stress particles in the SPH simulation. The Young's modulus and Poisson's ratio of the disc specimen are 1.375 GPa and 0.285. Comparisons between the numerical results and the analytical solutions of the stress distribution along the y axis are shown in Fig. S3. The stress contours are shown in Figs. S4a and S4b. The numerical simulation is coincident with the analytical solution, indicating that the SPH method is feasible.

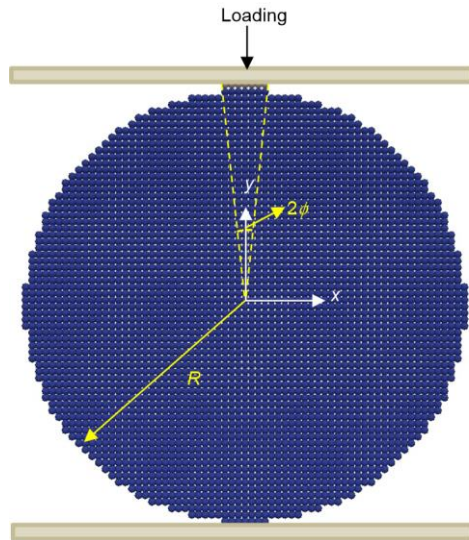


Fig. S1 SPH simulation setup of the Brazilian disc model

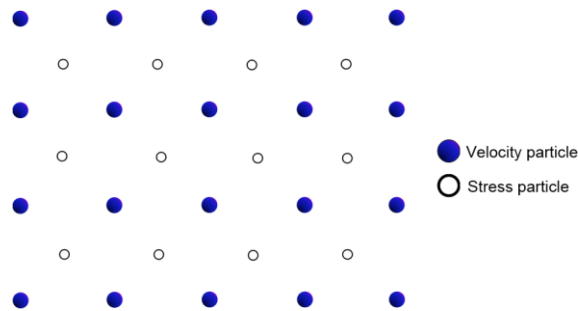


Fig. S2 Velocity particles and stress particles arrangement in a SPH simulation

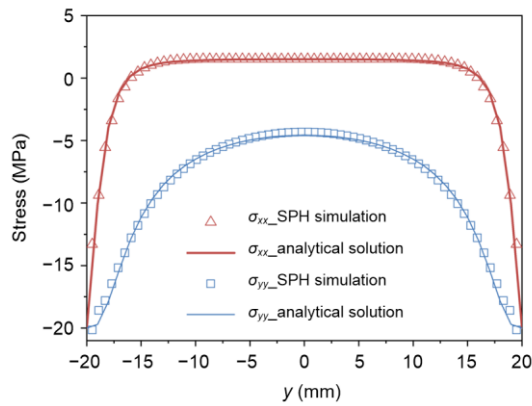


Fig. S3 Comparisons of SPH modeling results and analytical solutions for the stress distribution along the y axis ($x=0$)

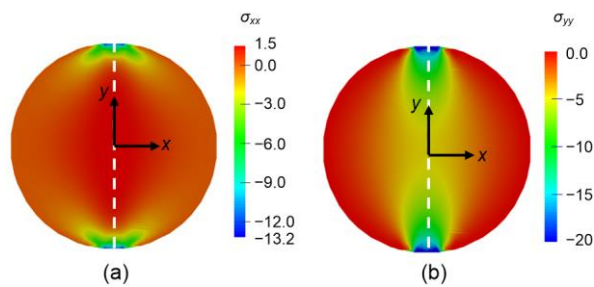


Fig. S4 Contour plot of (a) horizontal stress (MPa); (b) vertical stress (MPa)

S6.2 Penny-shaped crack

In this paper, the classical fracture mechanics problem of a flat elliptical crack in a rock medium is simulated. In 2D calculation, it is a line crack problem in the center of a plate. The medium is not subjected to external force, and the crack surface is subjected to a constant pressure p to make the crack open. Sneddon (1946) gave the analytical solution of horizontal stress distribution along the x axis in the plate under the condition of plane strain:

$$\sigma_{xx}(x,0) = p \left(\frac{|x|}{\sqrt{x^2 - c^2}} - 1 \right), \quad (\text{S13})$$

in which x is the x -coordinate of the calculation point in the plate, c is the half length of the initial crack.

Fig. S5 depicts the SPH setup of the penny-shaped crack model. The plate size is 5 m×5 m. There is a horizontal initial crack in the center of the plate with a length of 0.4 m. The SPH model is established with an initial particle spacing of 0.05 m and a total particle number of 10192. Assuming that the plate material is linear elastic, the Young's modulus and Poisson's ratio of the disc specimen are 26.7 GPa and 0.2. The pressure on the crack surface is 20 MPa. Comparisons between the numerical results and the analytical solutions of the stress distribution along the x axis are shown in Fig. S6. The numerical simulation fits well with the analytical solution, verifying the accuracy of the SPH method in simulating a crack problem.

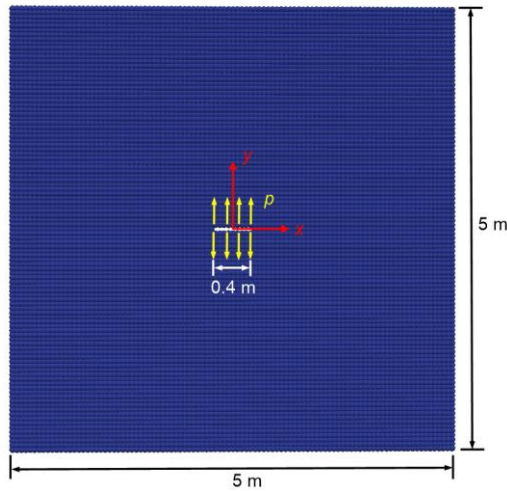


Fig. S5 SPH simulation setup of the penny-shaped crack model

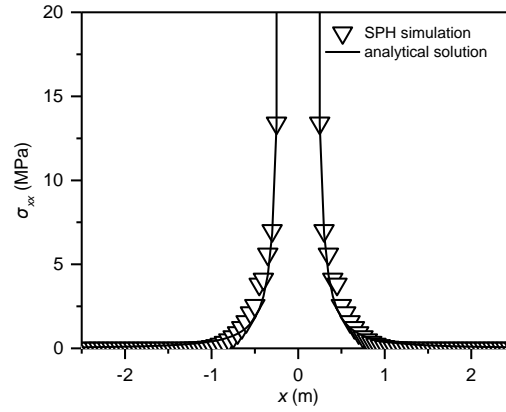


Fig. S6 Comparisons of SPH modeling results and analytical solutions for the stress distribution along the x axis ($y=0$)

S7 The convergence study

To verify the convergence of the simulation, different particle discretization sizes are used for the unfilled flawed disc ($\theta=45^\circ$) simulation, and the peak loads and errors obtained are tabulated in Table S1, in which Δd represents the initial particle space of the model. Under the three different spatial discretization sizes, the peak loads obtained in the simulation coincide with the experiment. Therefore, it is shown that the SPH simulation has met the convergence requirement. Since the failure analysis in this paper mainly focuses on the disc part, and not on the filling material part, the particle distance setup, 0.6 mm, is feasible and can be used in follow-up studies.

Table S1 Comparisons of peak loads with different spatial discretization sizes

Test cases	Velocity particle number	Stress particle number	Peak load (kN)	Error
Experiment	—	—	1.10	—
$\Delta d=0.6$ mm (SPH)	3487	3462	1.05	4.5 %
$\Delta d=0.45$ mm (SPH)	6195	6156	1.06	3.6%
$\Delta d=0.3$ mm (SPH)	13853	13758	1.06	3.6%

The smoothing length affects the accuracy of calculation and an excessive smoothing length will lead to large errors in particle results near the boundary. In this paper, in order to validate the rationality of the smoothing length, three different smoothing lengths have been selected for simulating the same unfilled flawed disc ($\theta=45^\circ$) model with the initial particle spacing of 0.6 mm. It can be seen from Table S2 that the smoothing length, $1.2\Delta d$, is reasonable and can be used for subsequent calculations.

Table S2 Comparisons of peak loads with different smoothing lengths

Smoothing length	Peak load (kN)	Error
Experiment	1.10	—
$1.0\Delta d$	0.95	13.6 %

$1.2\Delta d$	1.05	4.5%
$1.5\Delta d$	1.05	4.5%

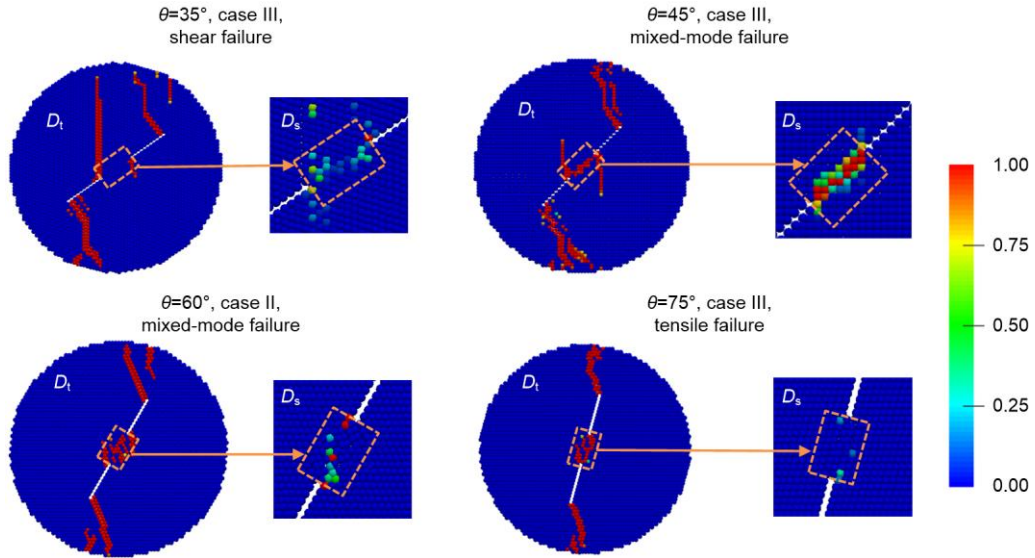


Fig. S7 Final failure patterns of disc specimens with different crack coalescence modes

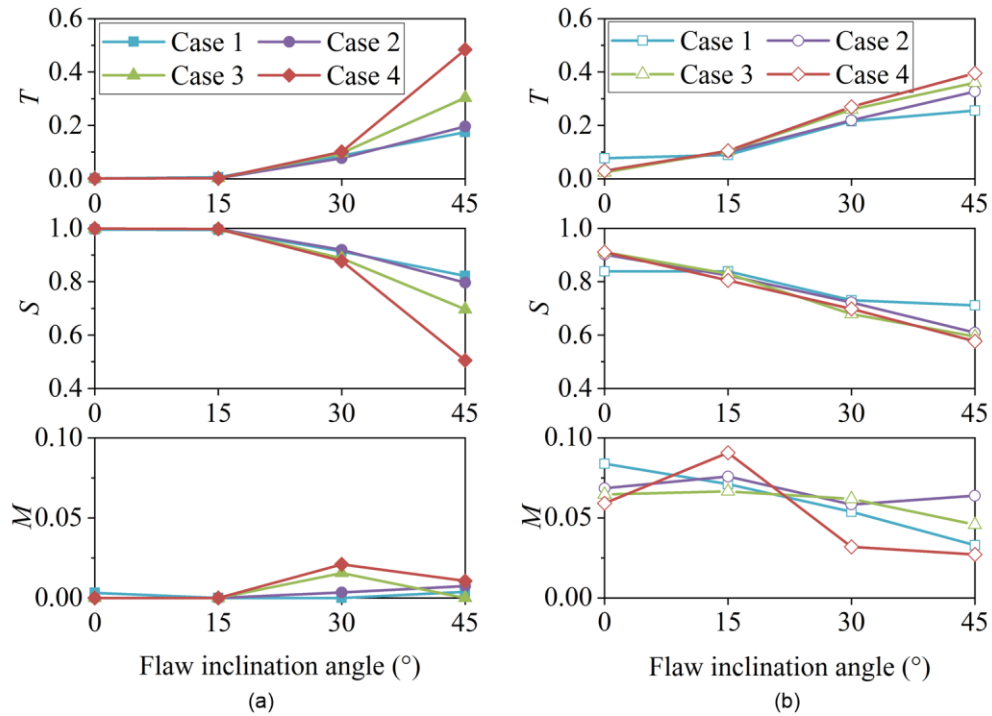


Fig. S8 Proportions of particle numbers in tensile damage state, shear damage state and mixed-mode damage state to the total number of damaged particles versus flaw inclination angle in disc specimens with filled flaws: (a) T , S , and M at peak load; (b) T , S , and M at post-failure

S8 The failure pattern analysis of the uniform distributed filling disc

For filled flaws disc specimens with θ less than 45° , the tensile and shear failure patterns show little difference when the filling material is different. They are all through-running failure

bands initiating from the center of the disc specimens. The typical failure contours (Case 3) are plotted in Fig. S9. In Fig. S9d, there is generation of wing cracks for $\theta=45^\circ$ and, in addition, there is an obvious failure band through the middle of the disc. For all cases shear damage is mainly concentrated at the filled flaws and the loading ends of the disc for all the cases, while in the case of $\theta=45^\circ$, there is some shear damage found at the position of the wing cracks generating from the filled flaw tips. That is consistent with the analysis in Section 4.2.1.1.

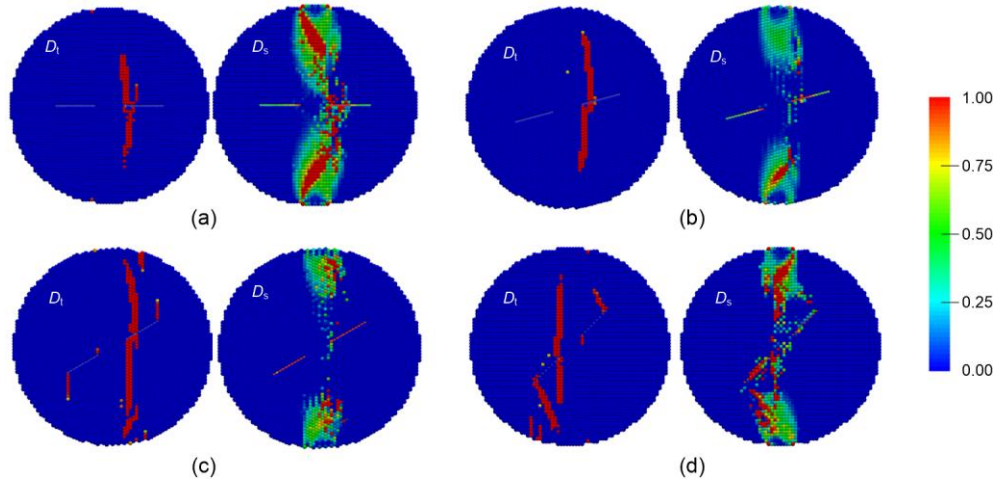


Fig. S9 Failure contours of disc specimens with filled flaws (case 3) in SPH simulations: (a) $\theta=0^\circ$; (b) $\theta=15^\circ$; (c) $\theta=30^\circ$; (d) $\theta=45^\circ$

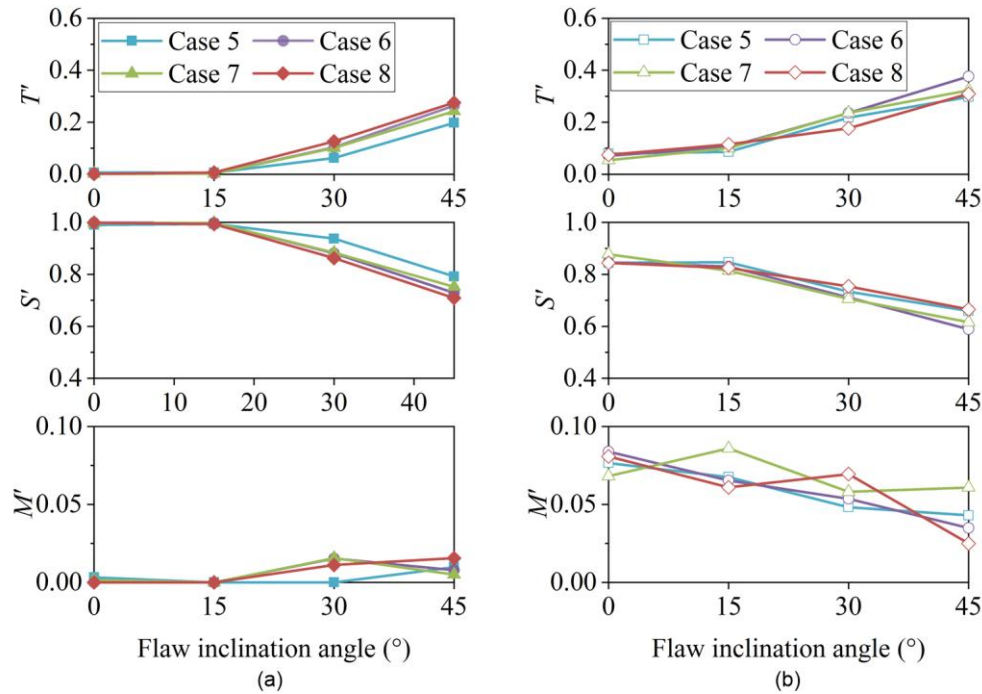


Fig. S10 Proportions of particle numbers in tensile damage state, shear damage state and mixed-mode damage state to the total number of damaged particles versus the flaw inclination angles in specimens with filled flaws: (a) T' , S' , and M' at peak load; (b) T' , S' , and M' at post-failure

S9 The failure pattern analysis of the non-uniform distributed filling disc

The difference of strength on the left and right flaws does not affect the appearance of the main crack generating from the center area of the disc specimens to the loading ends. The characteristic failure contours (Case 6) are plotted in Fig. S11. In Fig. S11d, for $\theta=45^\circ$, the

difference in fillings' strength between the left and right flaws makes the cracking paths of the disc specimen more complex. In addition to the through-running failure band along the central line of the disc, there are obvious mixed-mode wing cracks generated at the tips of the weaker filled flaw. With θ of the disc specimen increasing close to 45° , the effect of the non-uniform distribution of the flaw-fillings is gradually enhanced, in which case wing cracks are more likely to appear. That is consistent with the analysis of Section 4.2.2.1.

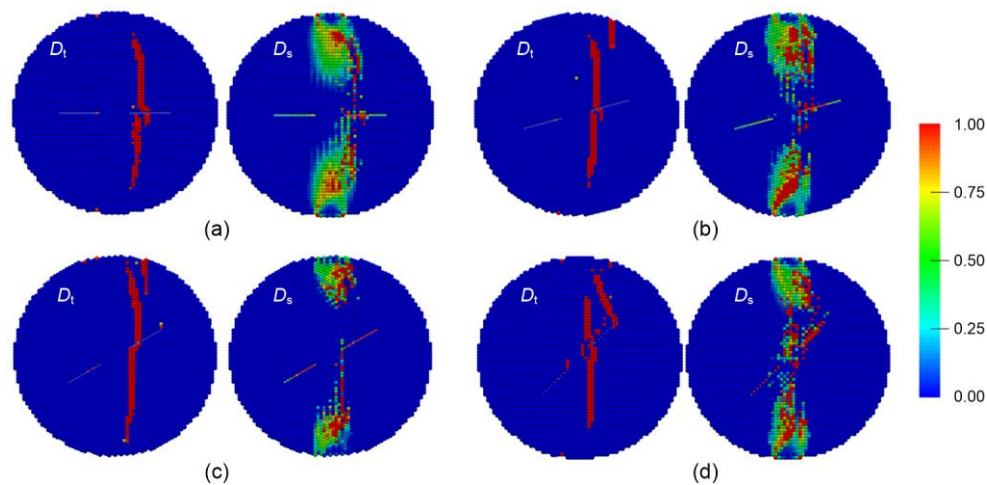


Fig. S11 Failure contours of disc specimens with filled flaws (Case 6) in SPH simulations (a) $\theta=0^\circ$; (b) $\theta=15^\circ$; (c) $\theta=30^\circ$; (d) $\theta=45^\circ$

References

- Belytschko T, Guo Y, Liu WK, et al., 2000. A unified stability analysis of meshless particle methods. *International Journal for Numerical Methods in Engineering*, 48(9):1359-1400.
[https://doi.org/10.1002/1097-0207\(20000730\)48:9<1359::AID-NME829>3.0.CO;2-U](https://doi.org/10.1002/1097-0207(20000730)48:9<1359::AID-NME829>3.0.CO;2-U)
- Belytschko T, Xiao SP, 2002. Stability analysis of particle methods with corrected derivatives. *Computers & Mathematics with Applications*, 43(3-5):329-350.
[https://doi.org/10.1016/S0898-1221\(01\)00290-5](https://doi.org/10.1016/S0898-1221(01)00290-5)
- Dyka CT, Randles PW, Ingel RP, 1997. Stress points for tension instability in SPH. *International Journal for Numerical Methods in Engineering*, 40(13):2325-2341.
[https://doi.org/10.1002/\(SICI\)1097-0207\(19970715\)40:13<2325::AID-NME161>3.0.CO;2-8](https://doi.org/10.1002/(SICI)1097-0207(19970715)40:13<2325::AID-NME161>3.0.CO;2-8)
- Hondros G, 1959. The evaluation of Poisson's ratio and the modulus of materials of low tensile resistance by the Brazilian (indirect tensile) test with particular reference to concrete. *Austrian Journal of Applied Science*, 10(3):243-268.
- Libersky LD, Petschek AG, Carney TC, et al., 1993. High strain lagrangian hydrodynamics: a three-dimensional SPH code for dynamic material response. *Journal of Computational Physics*, 109(1):67-75.
<https://doi.org/10.1006/jcph.1993.1199>
- Monaghan JJ, 2005. Smoothed particle hydrodynamics. *Reports on Progress in Physics*, 68(8):1703-1759.
<https://doi.org/10.1088/0034-4885/68/8/R01>
- Monaghan JJ, 2000. SPH without a tensile instability. *Journal of Computational Physics*, 159(2):290-311.
<https://doi.org/10.1006/jcph.2000.6439>
- Rabczuk T, Belytschko T, Xiao SP, 2004. Stable particle methods based on Lagrangian kernels. *Computer Methods in Applied Mechanics and Engineering*, 193(12-14):1035-1063.

<https://doi.org/10.1016/j.cma.2003.12.005>

Sneddon IN, 1946. The distribution of stress in the neighbourhood of a crack in an elastic solid. *Proceedings of the Royal Society A, Mathematical, Physical and Engineering Sciences*, 187(1009):229-260.

<https://doi.org/10.1098/rspa.1946.0077>

Vignjevic R, Campbell J, Libersky L, 2000. A treatment of zero-energy modes in the smoothed particle hydrodynamics method. *Computer Methods in Applied Mechanics and Engineering*, 184(1):67-85.

[https://doi.org/10.1016/S0045-7825\(99\)00441-7](https://doi.org/10.1016/S0045-7825(99)00441-7)